
On phase change and latent heat models in metal additive manufacturing process simulation

S. D. Proell · W. A. Wall · C. Meier

Abstract This work proposes an extension of phase change and latent heat models for the simulation of metal powder bed fusion additive manufacturing processes on the macroscale and compares different models with respect to accuracy and numerical efficiency. Specifically, a systematic formulation of phase fraction variables is proposed relying either on temperature- or enthalpy-based interpolation schemes. Moreover, two well-known schemes for the numerical treatment of latent heat, namely the apparent capacity and the so-called heat integration scheme, are critically reviewed and compared with respect to numerical efficiency and overall accuracy. Eventually, a novel variant of the heat integration scheme is proposed that allows to directly control efficiency and accuracy by means of a user-defined tolerance. Depending on the chosen tolerance, it is shown that this novel approach offers increased numerical efficiency for a given level of accuracy or improved accuracy for a given level of numerical efficiency as compared to the apparent capacity and the original heat integration scheme. The investigation and comparison of all considered schemes is based on a series of numerical test cases that are representative for application scenarios in metal powder bed fusion additive manufacturing.

Keywords latent heat · phase change · heat transfer · metal additive manufacturing · numerical simulation · finite element method

1 Introduction

Additive manufacturing (AM) is widely considered to be a key technology for future advances in engineering. AM offers highest flexibility in part design while still achieving the mechanical properties required for functional parts [9]. In metal powder bed fusion additive manufacturing (PBFAM) multiple layers of metal powder are successively molten at selected positions, which eventually form the cross-sections of the final part after solidification. Energy is commonly

deposited by a laser or electron beam giving rise to the respective names selective laser melting (SLM) and electron beam melting (EBM). These processes come with very challenging thermophysical phenomena on multiple length and time scales [15]. Accordingly, existing modeling approaches can be classified with respect to the resolved length scales: Macroscale approaches commonly aim at determining spatial distributions of physical fields such as temperature, residual stresses or dimensional warping on the scale of the design part. Mesoscale approaches resolve the length scale of individual powder particles on domains smaller than one powder layer to either study the melt pool thermo-fluid dynamics during the melting process [20, 23, 25, 38, 42, 43] or the cohesive powder flow during the previous powder recoating process [14, 27, 28]. Last, microscale approaches predict the evolution of the metallurgical microstructure during solidification [10, 24, 33, 39, 45]. A broad overview of state-of-the-art modeling approaches on these different length scales can be found in [26]. The present article focuses on the development of a thermal macroscale model for metal PBFAM processes.

Macroscale PBFAM models typically treat the powder phase as a homogenized continuum described via effective, i.e., spatially averaged, thermal and mechanical properties, without resolving individual powder particles. Also, the complex fluid dynamics within the melt pool are typically not explicitly resolved. Instead, a pure thermo-(solid-)mechanical problem is solved, usually based on a Lagrangean description and a spatial finite element discretization, with specific temperature- and phase-dependent thermal and mechanical constitutive parameters for the (homogenized) powder phase, the melt phase and the solidified phase. On the one hand, from a modeling point of view, such a procedure considerably simplifies the coupling of the different phase domains. On the other hand, this approach seems to be well-justified for certain simulations and quantities of interest since the mechanical forces transferred from powder and liquid phase

onto the solid phase are often negligible in good approximation.

In their works [11–13], Gusarov et al. proposed a model for powder bed laser absorption, which has been incorporated in many existing macroscale modelling approaches. For example, by using this absorption model, [16, 17] proposed a thermo-mechanical finite element (FE) model accounting for temperature- and phase-dependent thermal and mechanical constitutive behavior. Further developments in this field consider e.g. the accuracy of the physical model by adding additional physical effects such as residual stress relaxation [6], improved models for temperature and phase-dependent thermal conductivity of the powder [2, 4] and melt [40] phase, anisotropic conductivity [21], phase-dependent laser absorptivity [37], thermodynamically consistent constitutive modelling based on phase energies [1], or by explicitly modeling the melt pool fluid dynamics [19], an approach inspired by similar schemes in the context of laser and electron beam welding [3, 8, 34]. Another important aspect for macroscale PBFAM models is computational efficiency, which has been addressed, among others, by applying dynamic mesh adaptivity schemes [7, 22, 35, 46], code parallelization and load balancing techniques [31] as well as process layer agglomeration approaches [16, 44, 46].

The present work addresses two important aspects of macroscale PBFAM models, namely the modeling of phase change and latent heat effects. Concerning the first aspect, we propose phase fraction variables which allow to formulate temperature- and phase-dependent material parameters in phase transition regions by consistent interpolation of the single phase parameters. While the definition of phase fraction variables is often somehow hidden in existing works, the present contribution defines these phase fraction variables in a transparent and systematic manner. Moreover, as basis of these phase fraction variables, different interpolation strategies, e.g. temperature-based or enthalpy-based interpolation, are discussed in detail.

Concerning the modeling of latent heat effects, the two schemes that are most widely used in PBFAM models, namely the simple apparent (heat) capacity approach [5, 29, 30, 35] and the more involved heat integration method [17, 32, 36], will be investigated in the present work. It is known in the context of PBFAM process simulation that the specific choice of the latent heat model might considerably influence the overall efficiency of the numerical model [17]. In the present work, the two aforementioned schemes, namely the apparent capacity approach and the heat integration method, are critically reviewed and compared with respect to numerical efficiency and overall accuracy. Eventually, a novel variant of the heat integration scheme is proposed that allows to directly control efficiency and accuracy by means of a user-defined tolerance. Depending on the chosen tolerance, it is shown that this novel approach offers increased numerical efficiency for

a given level of accuracy or improved accuracy for a given level of numerical efficiency as compared to the apparent capacity and the original heat integration scheme. To isolate the effects of interest, the present study is restricted to purely thermal problems with length and time scales characteristic for PBFAM.

This article is structured as follows: Section 2 summarizes the mathematical problem statement and introduces the heat source modeling of a laser beam. The general numerical solution procedure is outlined in Section 3. Next in Section 4 temperature-history dependent material parameters are interpolated on the basis of properly defined phase fraction variables that allow to distinguish powder, solid and melt phase. The treatment of latent heat associated with phase change problems is considered in detail with the two mentioned methods, namely the apparent capacity and the heat integration scheme, and eventually the novel tolerance-based variant of the heat integration scheme is proposed. Numerical experiments are presented in Section 5 with a focus on accuracy and efficiency of the considered methods. A short conclusion is provided in Section 6.

2 General thermal model

For the purpose of this study it is sufficient to focus on the following instationary thermal problem described by the heat equation and appropriate boundary conditions:

$$\begin{aligned} C(T)\dot{T} + \nabla \cdot \mathbf{q} &= \hat{r}, & \text{in } \Omega, \\ T &= \hat{T}, & \text{on } \Gamma_T, \\ \mathbf{q} \cdot \mathbf{n} &= \hat{q}, & \text{on } \Gamma_q. \end{aligned} \quad (1)$$

Temperatures T are prescribed on the boundary part Γ_T and heat fluxes on Γ_q . The heat flux \mathbf{q} is specified by Fourier's law for isotropic material,

$$\mathbf{q} = -k(T) \nabla T. \quad (2)$$

Material properties, namely (volumetric) heat capacity C and conductivity k , depend on temperature but also on phase. The modeling of these parameters and the introduction of the phase change problem are found in Section 4.

The source term \hat{r} is used to model the deposited energy, here achieved by a laser beam, as a volumetric heat source based on Gusarov et al. [13]. This model for the laser source term is derived by considering radiative and conductive properties of the powder material. A summary of the resulting model is given here without stepping through the rather involved derivations. Let a powder layer be distributed in the xy -plane, where the powder material extends in positive z -direction from the powder layer surface at $z = 0$ up to the layer thickness L at $z = L$ (see also Fig. 15). A laser beam of nominal power W and size R is applied normal to this plane.

The source term is then given in a local coordinate system relative to the laser beam center by

$$\hat{r}(r_h, z) = -\beta_h Q_0 \frac{\partial q}{\partial \xi'}, \quad (3)$$

where r_h is the distance in the xy -plane from the laser beam center and β_h is the extinction coefficient. The nominal power density Q_0 is radially distributed around the laser beam center as

$$Q_0 = \begin{cases} \frac{3W_e}{\pi R^2} \left(1 - \frac{r_h}{R}\right)^2 \left(1 + \frac{r_h}{R}\right)^2, & 0 < r_h < R \\ 0, & \text{otherwise} \end{cases}. \quad (4)$$

The nominal laser power W has been averaged and reduced to an effective power W_e to account for various losses. Thus, (4) describes the spatial distribution in x - and y -direction. The normalized power density q is given in terms of the dimensionless coordinate $\xi' = \beta_h z$ as

$$q = \frac{\rho_h a}{(4\rho_h - 3)D} \left\{ e^{-\lambda} (1 - \rho_h^2) \left[e^{-2a\xi'} (1 - a) + e^{2a\xi'} (a + 1) \right] - \left[e^{2a(\lambda - \xi')} (1 - a - \rho_h(a + 1)) + e^{2a(\lambda - \xi')} (a + \rho_h(a - 1) + 1) \right] (\rho_h e^{-2\lambda} + 3) \right\} - \frac{3(1 - \rho_h)(e^{-\xi'} - \rho_h e^{\xi' - 2\lambda})}{4\rho_h - 3}, \quad (5)$$

with hemispherical reflectivity ρ_h , constant $a = \sqrt{1 - \rho_h}$, optical thickness $\lambda = \beta_h L$ and the constant

$$D = (1 - a) [1 - a - \rho_h(1 + a)] e^{-2a\lambda} - (1 - a) [1 + a - \rho_h(1 - a)] e^{2a\lambda}. \quad (6)$$

Apart from the optical properties, Eq. (5) only depends on the z -coordinate and specifies the power distribution in normal direction. The local coordinate system moves with the laser beam along a defined scanning track with velocity v .

3 Numerical solution procedure

Governing equation (1) is discretized in space with the finite element method (FEM). In the scope of the present work, linear shape functions are employed. Time is discretized with a one-step theta time integration scheme. Together this yields a fully discrete, nonlinear system of equations for the discrete temperatures T_j^n , where j is the nodal index of the FEM discretization and n the time step index. The equations are nonlinear due to the subsequently discussed temperature-dependence of heat capacity and conductivity as well as the yet to be introduced phase change subproblem. The discrete,

nonlinear problem is linearized and solved iteratively with a consistent Newton-Raphson method. All simulations are performed in the in-house research code BACI [41], a parallel, multi-physics finite element framework.

4 Modeling phase change and solidification

So far we have not addressed one crucial aspect of the specific thermal problem: the phase change, first from powder to liquid and eventually to solid phase. The general mathematical basis for phase change is briefly reviewed here. Suppose a domain contains both solid and liquid phase separated by the interface Γ_m which is defined by temperature T being at melting temperature $T = T_m$. At any point on the interface the so-called Stefan-Neumann equation has to hold:

$$\underbrace{\mathbf{n}_{sl} \cdot \left(k_s \frac{\partial T}{\partial \mathbf{x}} \Big|_s - k_l \frac{\partial T}{\partial \mathbf{x}} \Big|_l \right)}_{\Delta q_m} = H_m \mathbf{n}_{sl} \cdot \mathbf{v}_{sl} \quad \text{on } \Gamma_m, \quad (7)$$

where \mathbf{n}_{sl} is the interface normal vector, H_m the latent heat of melting and subscripts $(\cdot)_s$ and $(\cdot)_l$ denote quantities evaluated in solid or liquid phase, respectively. The absorbed or released heat flux Δq_m is proportional to the velocity \mathbf{v}_{sl} of the evolving interface. Equation (7) makes it clear that the temperature gradients and heat fluxes are in general discontinuous at the phase interface.

Equation (7) takes the form of a free boundary condition. An alternative formulation is obtained by multiplying it with a differential surface element $d\Gamma$, which yields

$$\Delta q_m d\Gamma = H_m \frac{dV}{dt}. \quad (8)$$

Equation (8) states that the absorbed or released differential heat $\Delta q_m d\Gamma$ is proportional to the volume change of either phase with a proportionality factor equal to the latent heat H_m . This formulation will prove to be useful since it is phrased in terms of volumes and not on the phase change interface.

The introduced Stefan-Neumann equation is formulated for elementally pure materials where phase change takes place at a fixed melting temperature. The temperature of a point on the interface will change only after all latent heat has been absorbed or freed. We will refer to this as isothermal phase change. For alloys, phase change typically happens in a rather narrow temperature interval between solidus temperature T_s and liquidus temperature T_l . In this case temperature gradually changes from T_s to T_l , reaching liquidus (solidus) temperature when all latent heat has been absorbed (released). We will refer to this as mushy phase change.

In this contribution the phase interface is implicitly defined by isotherms, a common choice in the context of PB-FAM process simulation. Depending on the type of phase change (isothermal or mushy) one might take the isotherm

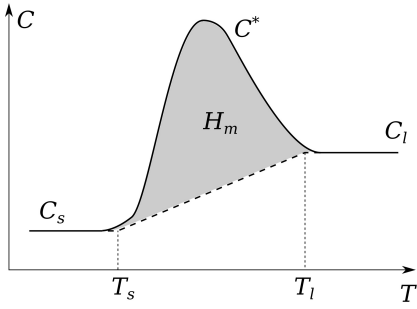


Fig. 1 Illustration of the apparent heat capacity method. The modified capacity C^* includes the effects of latent heat H_m in an integral sense.

at melting temperature or both isotherms at solidus and liquidus temperature to represent the phase interface. Other approaches include explicit interface tracking e.g. with level set schemes and discrete solution spaces provided by enriched or extended finite element approaches. Instead of a sharp boundary the interface can also be tracked by means of an explicit phase variable that changes over an interface of finite thickness [26].

4.1 Modeling effects of latent heat

Hu and Argyropoulos [18] review various methods to account for the latent heat H_m associated with phase change. In the following sections two popular methods are briefly presented and then modified with the target application in mind.

4.1.1 Apparent capacity method

One of the simplest approaches is the so-called *apparent capacity* (AC) method. We will first introduce it for mushy phase change. The idea is to artificially increase the heat capacity C in the melting region in such a way that an increased amount of energy is necessary in the model to heat the material. This increased energy shall be equal to the latent heat H_m . Expressed mathematically, this means

$$\int_{T_s}^{T_l} C_{\text{app}} dT = \int_{T_s}^{T_l} C(T) dT + H_m, \quad (9)$$

where C_{app} is the modified capacity. The shape of the modified capacity function can in principle be chosen freely. A common choice is to set it to a constant in the phase change region with a jump discontinuity at solidus and liquidus temperature. In [5] this approach is used in combination with an averaging technique. In this contribution a C^1 -continuous smoothed triangular distribution as shown in Fig. 1 is used for an improved Newton convergence.

It is also possible to apply the AC method to isothermal phase change happening at melting temperature T_m . In this case artificial temperatures $T_s = T_m - d$ and $T_l = T_m + d$ are introduced, which gives a nonphysical phase change interval

of width $2d$. The isothermal phase change will hence conceptually be modeled as mushy. If one is interested in an accurate representation of temperatures around the melting point, the width should be chosen small. However, in terms of an energy balance the same amount of latent heat H_m will be absorbed or released after the respective phase change completes due to the definition in (9).

As simple as the AC method may be, it suffers from a major drawback. When temperature increments are too large in one time step, the solution temperature might only capture part of or even step over the increased capacity peak. Consequently, phase change is not considered correctly in the sense of an energy balance.

4.1.2 Heat integration method

Another popular and more advanced procedure is what Hu and Argyropoulos [18] call the *heat integration* (HI) method. It has first been applied to a FE setting by Rolph and Bathe [36] and is still used in more recent contributions [17,32]. In short, the method adds an additional source term to the discrete, linearized form of governing equation (1) in each nonlinear iteration step. In the first iteration step the system is solved as usual. In each subsequent iteration i an artificial source term q_p^{i-1} determined from the previous iterate is added to the thermal residual. The Jacobian is not changed and thus the modified thermal residual is no longer consistently linearized.

Original method We will first introduce our understanding of the original HI method [36] to calculate the source term. The specific notation was inspired by the formulation in [32]. Starting from the control volume formulation of the Stefan-Neumann equation (8), an incremental source term Δq_p^i is defined for iteration step i along with the total latent heat available $q_{p,\text{tot}}$:

$$\Delta q_p^i = - \int_{\Omega} \frac{1}{\Delta t} C (T^i - T_m) d\Omega, \quad (10)$$

$$q_{p,\text{tot}} = - \int_{\Omega} \frac{1}{\Delta t} H_m d\Omega, \quad (11)$$

where the index $(\)_p$, for phase change, distinguishes these quantities from heat fluxes. Originally, the negative sign corresponds to a melting problem although our algorithm can also handle solidification, as we will see later. The term (10) can be interpreted as a penalty for stepping over the melting temperature T_m . The idea is to add these terms, which represent latent heat, until the current temperature T^i stays at a consistent melting temperature T_m . Alternatively, when the sum of all increments ever applied reaches the allowed total in (11), no more increments are added and the temperature is allowed to deviate from the melting temperature again.

For simplicity the terms are formulated for isothermal phase change.

Compared to typical FE integrals, equations (10) and (11) are evaluated at nodes and not at element integration points. For this purpose, the nodal lumped pseudo-mass \tilde{m}_j is defined for a node j as

$$\tilde{m}_j = \sum_k \int_{\Omega} N_j N_k d\Omega \quad (12)$$

with the FE shape functions N_j and N_k . This looks very similar to a lumped mass matrix ubiquitous in FEM. Scaling (12) with a constant density ρ would give a nodal mass (hence the naming pseudo-mass), scaling with C gives a nodal capacity. The lumped pseudo-mass \tilde{m}_j can be computed in the beginning of a simulation and is assumed constant throughout. The total latent heat available can now be computed in the beginning for each node j as

$$q_{p,j,tot} = -\frac{1}{\Delta t} H_m \tilde{m}_j, \quad (13)$$

which is the lumped version of (11). Each node stores a history-variable $q_{p,j}^{hist}$ accumulating the amount of latent heat that has been absorbed over the whole simulation. It is initialized as zero for solid material. After each Newton iteration i in time step $n+1$ the following calculations are performed:

1. Skip node j if

$$\begin{aligned} & [T_{j,n+1}^i < T_s \text{ and } T_{j,n} < T_s] \text{ or} \\ & [T_{j,n+1}^i > T_l \text{ and } T_{j,n} > T_l] \end{aligned} \quad (14)$$

which means it is not undergoing phase change. In this case the source term increment $\Delta q_{p,j}^i$ is set equal to zero. Here, $T_{j,n}$ denotes the converged temperature value of node j at the last time step n .

2. Else, for each node j which is undergoing phase change compute the increment

$$\Delta q_{p,j}^i = -\frac{1}{\Delta t} C^* (T_{j,n+1}^i - T^*) \tilde{m}_j, \quad (15)$$

which is the lumped version of (10). Here, T^* is an intermediate temperature given by

$$T^* = T_s + \left| \frac{q_{p,j}^{hist}}{q_{p,j,tot}} \right| (T_l - T_s), \quad (16)$$

calculated from the amount of latent heat already absorbed (released) during melting (freezing). The modified capacity is computed as

$$C^* = \left(\frac{T_l - T_s}{H_m} + \frac{2}{C_s + C_l} \right)^{-1}, \quad (17)$$

where C_s and C_l are the values of heat capacity at T_s and T_l , respectively. In case of isothermal phase change,

the intermediate temperature simplifies to the melting temperature, i.e. $T^* = T_m = T_s = T_l$, and the modified capacity simplifies to the averaged capacity at the melting point, i.e. $C^* = \frac{1}{2}(C_s + C_l)$.

3. Limit each increment $\Delta q_{p,j}^i$ such that the following condition is fulfilled:

$$0 \geq q_{p,j}^{hist} + \Delta q_{p,j}^i \geq q_{p,j,tot}. \quad (18)$$

The last increment (before phase change is completed) is limited such that the respective bound is exactly reached. Afterwards add it to the history $q_{p,j}^{hist} \leftarrow q_{p,j}^{hist} + \Delta q_{p,j}^i$.

4. For each node j where $|\Delta q_{p,j}^i| > 0$ reset the temperature

$$T_{j,n+1}^i = T^*. \quad (19)$$

5. Calculate the total source term as the sum of all increments from previous iterations within this time step,

$$q_{p,j}^i = \sum_{k=0}^i \Delta r_{p,j}^k, \quad (20)$$

where the first iteration in each time step starts with a vanishing source term, i.e. $q_{p,j}^0 = 0$.

It is again emphasized that the history value $q_{p,j}^{hist}$ in (18) accumulates enthalpy increments $\Delta q_{p,j}^i$ over the whole simulation, i.e. over all nonlinear iteration steps in all time steps, while the source term in (20) only accumulates the increments $\Delta q_{p,j}^i$ over all iterations of the current time step $n+1$.

This method ensures that phase change is captured accurately: the thermal residual is modified and at the same time the temperature is fixed to a consistent value until all latent heat has been absorbed or released. Limiting condition (18) allows to use the same algorithm for both melting and solidification as discussed at the end of this section. As noted by the authors of the original work [36], the HI method requires the consistent use of the nodal lumped capacity. Thus, when using this algorithm, the capacity matrix must enter the residual and Jacobian in Newton's method in lumped form to obtain a robust scheme. Nevertheless, the original HI method converges slowly due to the inconsistent modification of the residual. This was already noted by [17] and [18]. As a remedy we propose a tolerance-based HI method in the following paragraph.

Tolerance-based method So far the number of iterations needed in the nonlinear solution procedure of one time step is only determined by the standard tolerance of Newton's method. We propose to introduce another tolerance to control the accuracy of the phase change representation. Hence, we stop adding increments when they are small compared to the total latent heat, i.e.,

$$\left| \frac{\Delta q_{p,j}^i}{q_{p,j,tot}} \right| < \epsilon_{tol}. \quad (21)$$

where $\varepsilon_{\text{tol}} < 1$ is a relative tolerance and describes the relative amount of latent heat which is not absorbed (released) after melting (solidification) is complete. Inserting (13) and (15) into (21) yields an alternative for step 1:

1.* Skip node j if

$$|T_{j,n+1}^i - T^*| < \varepsilon_{\text{tol}} \frac{H_m}{C^*}. \quad (22)$$

The new criterion provides a way to stop HI when a certain accuracy is achieved. At first glance this seems to significantly change the outcome of the algorithm since (15) will be evaluated for nodes that are far away from a phase change. However, the limiting condition (18) will automatically neglect all nodes that are not undergoing phase change as demonstrated in the following.

First, consider a node that is heated up and the material is undergoing a melting process. Initially, the node is in solid state, i.e. $q_{p,j}^{\text{hist}} = 0$, with a temperature below the solidus temperature, i.e. $T_{j,n+1}^i < T_s$. The calculated increment (15) would be positive. Since there is no phase change yet, no increment should be added. Indeed, limiting according to (18) will not allow a positive increment with a zero history and the increment is set to zero. When the temperature rises above the solidus temperature T_s , however, the increments become negative and will be considered according to (18). The history $q_{p,j}^{\text{hist}}$ accumulates negative increments until it reaches the allowed total $q_{p,j,\text{tot}}$, which by definition (13) is also negative. Then the material is fully molten.

Next, the phase change is reversed by cooling a node with material in the molten state. If material is molten, then $q_{p,j}^{\text{hist}} = q_{p,j,\text{tot}} < 0$. Looking at the limiting condition (18) shows that only positive increments are allowed, when material is molten. As expected, positive increments (15) are obtained, and the solidification process is initiated, as soon as temperature drops below the liquidus temperature T_l . The positive increments are added to the history $q_{p,j}^{\text{hist}}$ until it reaches zero. Then the material has returned to a solid state. The phase change as it was just described is fully reversible.

4.2 Temperature- and phase-dependent parameters

As common in macroscale PBFAM models, all three phases are modeled as pseudo-solid materials with varying material parameters. On the one hand, this procedure considerably simplifies the numerical schemes for coupling the different phases. On the other hand, this approach is justified since the mechanical forces transferred from powder and liquid phase onto the solid phase are negligible in good approximation for many questions. It is important to note that the powder phase does not represent a phase in the same sense as solid, liquid and gaseous state: once powder is molten it becomes a consolidated phase and can never return to powder state.

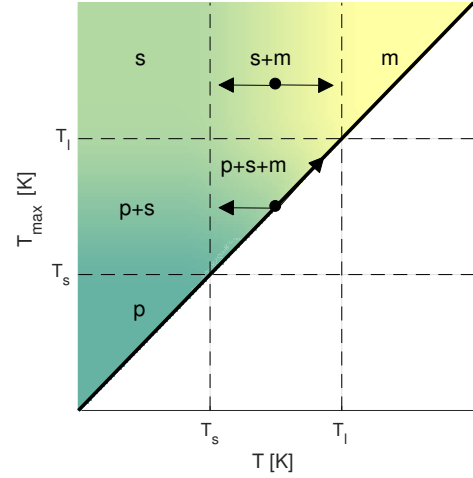


Fig. 2 Temperature history diagram illustrating the two-dimensional nature of material parameter interpolation between powder (p), melt (m) and solid (s). Arrows indicate possible movement within the diagram.

In the following we will expand on these considerations considering only mushy phase change for now.

Fig. 2 gives an illustration of the possible states of a material point. The current temperature T is on the ordinate, while the abscissa shows the highest temperature ever reached, T_{max} . The different areas correspond to different mixtures of powder, melt and solid. By definition there cannot be any possible state for $T > T_{\text{max}}$ and this area is blanked out. If $T_{\text{max}} < T_s$, all material must still be in powder form (p). If $T_{\text{max}} > T_l$, there is no more powder, all material is consolidated and thus must be solid (s) or molten (m). The exact constitution of the two then depends on the current temperature. The same reasoning applies to the current temperature. If $T > T_l$, all material must be molten. If $T < T_s$, material is a mixture of powder and solid, where the exact constitution is depending on T_{max} . Perhaps the most interesting scenario is obtained when $T_s < T < T_{\text{max}} < T_l$. In this case some powder is still left and the consolidated phase is made up of melt and solid. The arrows in Fig. 2 indicate the possible evolution of phases. Due to the definition of T_{max} the only way to increase its value is an irreversible movement along the black line in Fig. 2. For all other locations in the diagram a reversible horizontal movement is possible. With these considerations a temperature-based interpolation procedure for any material parameter can be derived.

Temperature-based interpolation First, the focus is on the transition from (non-powder) solid to melt. The liquid fraction g is introduced as

$$g(T) = \begin{cases} 0, & T < T_s \\ \frac{T-T_s}{T_l-T_s}, & T_s \leq T \leq T_l \\ 1, & T > T_l \end{cases} \quad (23)$$

If only solid and liquid phase were present, any material parameter f could be interpolated from the solid and melt values f_s and f_m . The history-dependent material behavior is captured by the fraction of consolidated material in time step $n + 1$ according to

$$r_c^{n+1} = \max[r_c^n, g(T)] \quad (24)$$

which is updated after each step and initialized with a proper start value r_c^0 (zero for powder, one for solid). For example, in a region that has initially been covered with powder, definition (24) equals the all-time maximum of the liquid fraction g at this location which, according to (23), carries the same information as the maximum temperature T_{\max} . In a region that has initially been covered with solid material, definition (24) equals one for all times since solid material can never transform back to powder. The monotonously increasing fraction of consolidated material r_c^{n+1} together with the liquid fraction g allow to define volume fractions for powder, melt and solid phases:

$$r_p^{n+1} = 1 - r_c^{n+1}, \quad (25)$$

$$r_m^{n+1} = g, \quad (26)$$

$$r_s^{n+1} = r_c^{n+1} - g. \quad (27)$$

Their physical motivation is as follows: The powder fraction r_p^{n+1} given in (25) is by definition the complement of the consolidated fraction r_c^{n+1} . The molten fraction r_m^{n+1} in (26) is independent of the history and is always determined by (23). The solid fraction r_s^{n+1} defined in (27) is the part of the consolidated fraction which is not molten. This also implies that in a material mixture containing solid and powder the solid fraction always melts first. With more history variables, also a different behavior could be realized (e.g. powder should melt first) but this is not deemed necessary in the context of macroscale PBFAM. Note that definitions (25), (26) and (27) satisfy partition of unity and are thus suitable for interpolation.

Any material parameter f can now be interpolated from the single phase values f_p, f_m, f_s weighted by the corresponding fractions

$$f(T) = r_p^{n+1}(T)f_p + r_m^{n+1}(T)f_m + r_s^{n+1}(T)f_s. \quad (28)$$

For the special choice $f_p = f_s$, a two phase interpolation without history-dependent behavior is recovered. The dependence on temperature is explicitly stated in (28) since this requires a consistent linearization to achieve robust convergence of the nonlinear solver. Fig. 3 shows the evolution of an exemplary material parameter f over the temperature history for the chosen liquid fraction definition (23). In the left diagram powder melts completely and consequently the parameter f takes on the value of a solid after cooling down below T_s . The right diagram shows partial melting: after cooling down below T_s the parameter is a weighted average of the

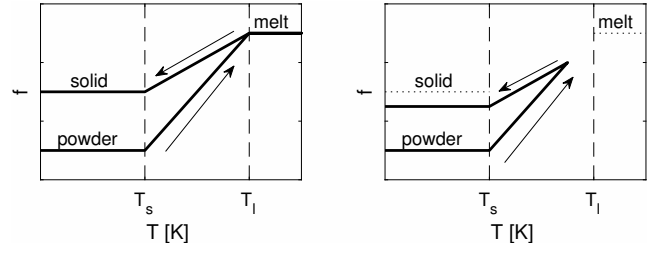


Fig. 3 Evolution of a material parameter depending on temperature history. Left: Material is completely molten and consolidated. Right: Temperature history stays below liquidus temperature and thus a fraction of material stays powder.

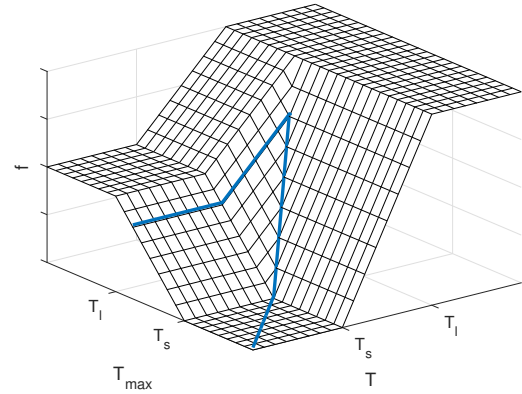


Fig. 4 Three-dimensional visualization of parameter interpolation. Material parameters are continuous in T and T_{\max} direction. The blue curve shows the evolution of the parameter when $T_{\max} < T_s$.

powder and solid value based on the consolidated fraction which is now smaller than 1. Fig. 4 shows the same interpolation in a three-dimensional representation which makes the history-dependence on T_{\max} more explicit and shows that the parameter interpolation is also continuous over the history. This is important in the modeling of PBFAM processes since it ensures a continuous transition of material parameters between regions of molten and solidified material and regions that are still covered with unmolten powder. Note that the definition of liquid fraction determines the exact shape of the interpolating curve (28). The kinks at T_s and T_l could also be smoothed out if this seemed necessary for robust Newton convergence.

Enthalpy-based interpolation In the case of isothermal phase change, the definition of liquid fraction based on temperature as in (23) will not work. A temperature-based parameter interpolation would still be possible based on a definition of solidus and liquidus temperature $T_s < T_m$ and $T_l > T_m$ as numerical regularization values rather than physically meaningful values. However, as a more consistent alternative approach the following formulation can be derived by rearrang-

ing (16) to read

$$\frac{T^* - T_s}{T_l - T_s} = \left| \frac{q_{p,j}^{\text{hist}}}{q_{p,j,\text{tot}}} \right|. \quad (29)$$

The fraction on the left-hand side is very similar to the liquid fraction (23). Thus, we may also interpret the right-hand side as a representation of the liquid fraction g_j of node j , i.e.

$$g_j = \left| \frac{q_{p,j}^{\text{hist}}}{q_{p,j,\text{tot}}} \right|, \quad (30)$$

which is guaranteed to be bounded between $[0, 1]$ due to the limiting condition (18). The liquid fraction in (30) is no longer formulated in temperatures but rather in latent heat. For an isothermal phase change, a change in latent heat directly corresponds to a change in enthalpy. Thus, the new fraction (30) can also be thought of as an enthalpy-dependent liquid fraction. All other parts of the interpolation procedure (28) remain unchanged. In the numerical examples, this liquid fraction based on latent heat will be employed in combination with the isothermal HI scheme. All schemes employing a finite phase change interval $[T_s; T_l]$, will use the temperature-based parameter interpolation with liquid fraction (23).

5 Numerical results

5.1 Solidification front in a 1D slab

To validate the implementation, first a series of numerical experiments are conducted on a one dimensional domain for which an analytic solution is available [18]. This example has already been used to show the validity of methods for capturing latent heat [5]. A pseudo one-dimensional slab (material properties of ice / water) with length $L = 1$ m is subject to a fixed temperature $\hat{T} = 253$ K on its left edge at $x = 0$. The initial temperature in the whole slab is $T_0 = 283$ K. The left part of Fig. 5 illustrates this scenario. The interface separating frozen and liquid water will slowly travel from left to right. Material parameters for water are given in Table 1, they are taken directly from [5]. The problem is discretized with 25, 50 or 100 linear finite elements in space and three different fixed step sizes $\Delta t \in \{200\text{s}, 400\text{s}, 800\text{s}\}$ in time. Total simulation time is $t_f = 72 \cdot 10^3$ s. At this point in time the temperature on the right edge is still at the initial level and the analytic solution (which is calculated on a semi-infinite domain) remains valid.

The introduced HI method will be used in four variants by distinguishing a) isothermal and mushy phase change as well as b) the original criterion (14) and the novel tolerance-based criterion (22). In this example, phase change of water is isothermal and thus the isothermal HI methods with either

Table 1 Material parameters of water [5] for Sections 5.1 and 5.2.

Parameter	Description	Value	Unit
T_m	Phase change temperature	273	K
H_m	Volumetric latent heat	338	MJ/m ³
C_s	Volumetric specific heat, solid	1.762	MJ/m ³ K
C_l	Volumetric specific heat, liquid	4.226	MJ/m ³ K
k_s	Thermal conductivity, solid	2.22	W/mK
k_l	Thermal conductivity, liquid	0.556	W/mK

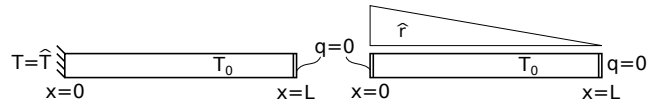


Fig. 5 Geometry, thermal loads, boundary and initial conditions for solidification front example (left) and melting volume example (right).

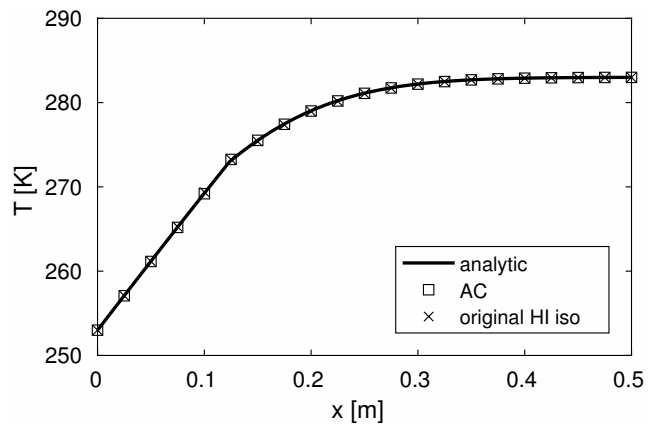


Fig. 6 Melting front example: Temperature profiles at t_f of analytic solution compared to numerical results with AC and HI method. 100 elements, $\Delta t = 200$ s.

original or tolerance-based criterion can be applied directly. For the AC method an artificial phase change interval is chosen with $T_s = 270$ K and $T_l = 276$ K, i.e., $d = 3$ K. The same interval is used to apply the original and tolerance-based mushy HI methods. Additionally, for tolerance-based HI the tolerance is chosen as $\epsilon_{\text{tol}} = 0.001$, i.e., up to 0.1% of latent heat will be neglected.

All approaches yield results that agree very well with the analytic solution. Fig. 6 shows the solutions obtained with AC and original isothermal HI method on the finest mesh as an example. The maximum errors in the numerical solutions provided by the different methods are shown for the three investigated meshes and time step sizes in Fig. 7. The maximum errors lie below 4% for the coarsest mesh and around 2% for the finer meshes, which is deemed accurate enough for the intended use case. Within the considered scope, the time step size seems to have only minor effect on the accuracy. All versions of HI schemes produce errors that are slightly higher compared to the error from the AC scheme. However, for the large time step sizes $\Delta t = 400$ s and $\Delta t = 800$ s the AC method does not always converge.

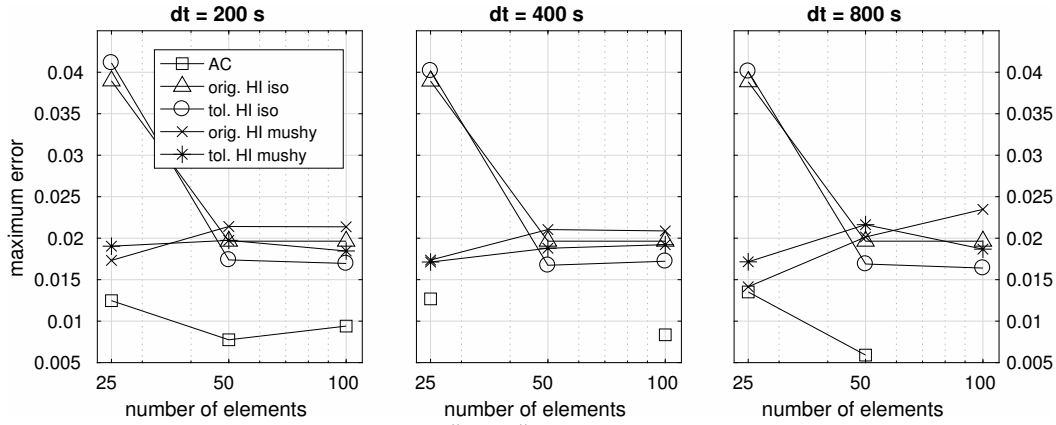


Fig. 7 Melting front example: Maximum error in temperature $\left\| \frac{T - T_{ref}}{T_0 - T} \right\|_{\infty}$ of different methods for latent heat depending on spatial and temporal discretization.

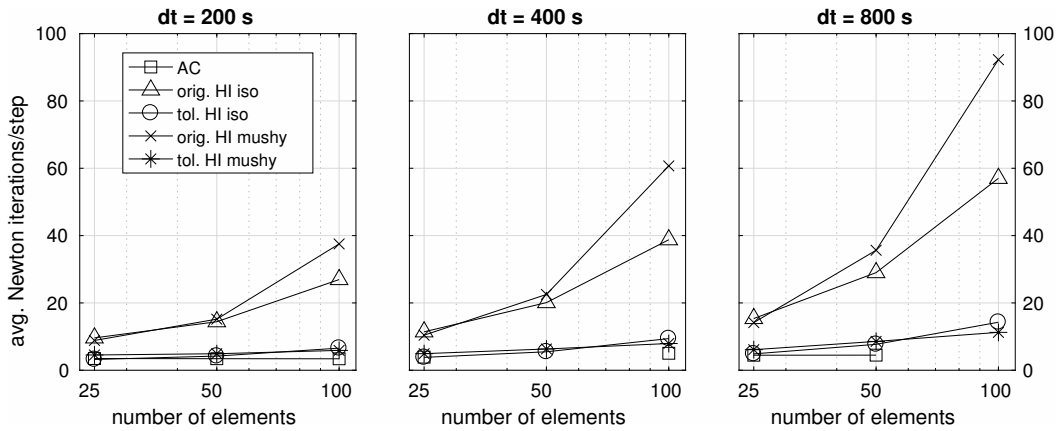


Fig. 8 Melting front example: Average number of nonlinear iterations of different methods for latent heat depending on spatial and temporal discretization.

The real difference between the methods comes to light when numerical efficiency is investigated in terms of Newton iterations needed per time step. Fig. 8 shows a strong dependence of the original HI method [36] on the spatial discretization with heavily increased iterations per time step in case of finer spatial resolution. On top of that a larger time step leads to a further increase in iterations. Both isothermal and mushy version of the original method suffer from this effect. Hodge et al. [17] mention that small time steps had to be used because of the original HI method. However, our proposed tolerance-based method does not only require significantly less iterations per step in every scenario but is also less sensitive to spatial and temporal discretization. This seems beneficial when moving to simulation of PBFAM processes on a part-scale.

5.2 Melting volume in a 1D slab

To get a better understanding of problem-dependency, we investigate the same variants on a slightly modified second example (Fig. 5, right). The Dirichlet condition on the left

boundary is dropped and all faces are assumed to be insulating. Instead a spatially varying source term $\hat{r} = 20,000(1 - x)^W/m^3$ is applied to the whole slab of water which is initially frozen at $T_0 = 263$ K. Material parameters for solid and liquid water are again given in Tab. 1. In contrast to the previous example, melting will not take place at a single node representing the phase interface. Instead a whole volume can be in phase transition (i.e. melting). The same spatial and temporal discretizations from before are used, total simulation time is $t_f = 20 \cdot 10^3$ s.

Again, the AC method and the four variants of HI are applied with the settings from above. No analytic solution is available for this scenario. Fig. 9 shows the obtained temperature profiles along the one dimensional slab for the fine discretization with 100 elements and a step size of 200s. Obviously, AC and mushy HI methods will not keep temperatures fixed at the melting temperature of 273 K during phase change. When one is concerned about exact representation of isothermal phase change, only the original and tolerance-based version of isothermal HI are accurate enough, although some oscillation around the melting temperature is observed.

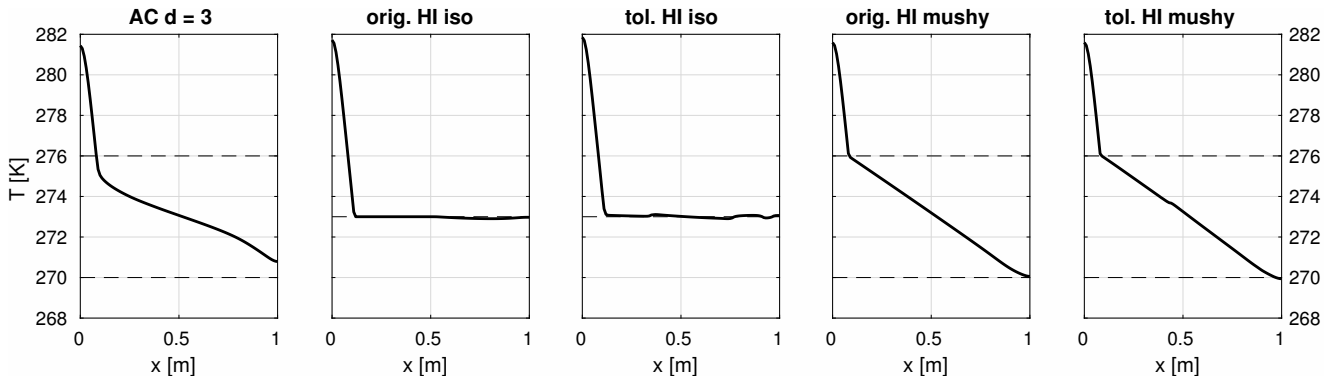


Fig. 9 Melting volume example: Temperature profiles at t_f obtained with five different methods for latent heat. 100 elements, $\Delta t = 200$ s.

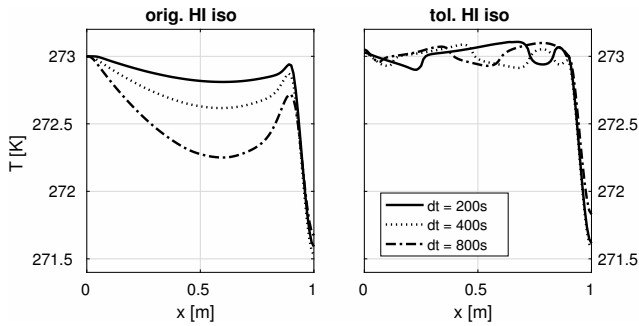


Fig. 10 Melting volume example: Temperature profiles at $0.5t_f$ obtained from the original and the proposed tolerance-based HI scheme (100 elements, time step varying).

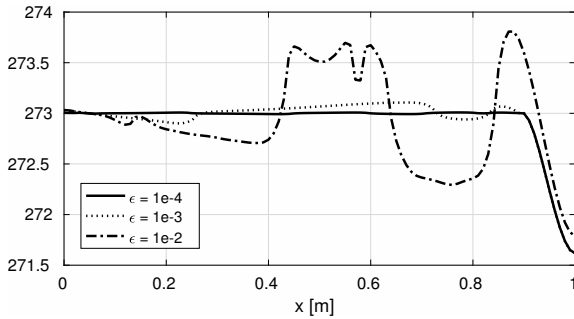


Fig. 11 Melting volume example: Temperature profiles at $0.5t_f$ obtained from the proposed tolerance-based HI scheme for different tolerances (100 elements, $\Delta t = 200$ s).

Looking at the final temperatures on the left edge, when melting is already finished, reveals that the latent heat of melting still is captured with good accuracy by all methods, and the predicted temperatures agree well. Given the large temperature range prevalent in the targeted application (PBFAM simulation on part-scale), a highly accurate representation of temperature profiles around the melting point is not of highest practical importance.

A short look on the accuracy of isothermal HI schemes is taken in this paragraph. Solutions with the HI scheme can become quite inaccurate around the melting temperature especially when larger time steps are used. Fig. 10 shows

such solutions of the original scheme at $t = 0.5t_f$ for different step sizes and compares it to our proposed tolerance-based method. Both methods cannot exactly enforce isothermal phase change which would be characterized by a horizontal plateau region at T_m . The original method's criterion (14) for determining nodes undergoing phase change proves to be ill-suited for this scenario. Larger time steps lead to larger undershoots in temperature. The fluctuations around melting temperature obtained with the proposed tolerance-based HI scheme on the contrary are independent of step size and only controlled by the tolerance ϵ_{tol} . The temperature profiles resulting from three different tolerances (0.01, 0.001 and 0.0001) can be seen in Fig. 11.

Next we turn to the efficiency of all methods and examine the average number of Newton iterations per time step shown in Fig. 12. Again, the original variants of the HI scheme need the most Newton iterations and are especially sensitive to temporal and spatial discretization. They are no longer considered in the remaining examinations. Fig. 13 only compares iterations of the AC and tolerance-based HI methods. The iteration count increases with increasing time step size for all three methods but stays more or less constant over all spatial discretizations. In the rightmost graph showing the largest time step, the AC for the first time requires more iterations than the proposed tolerance-based HI methods.

This melting volume example reveals an already mentioned problem of AC methods, namely the possibility to neglect much of latent heat by stepping over or passing through the phase change interval too fast. The AC method is used with three widths $d \in \{1 \text{ K}, 2 \text{ K}, 3 \text{ K}\}$ to compute artificial solidus and liquidus temperatures $T_s = T_m - d$ and $T_l = T_m + d$. The final temperature profiles are graphed in Fig. 14 for three time step sizes and the finest mesh with 100 finite elements. Obviously, the profiles differ in the respective phase change intervals which would not be the main concern in PBFAM. Instead focus lies on the maximum temperature predicted on the left edge. For the smallest time step $\Delta t = 200$ s all widths reach almost the same maximum temperature. Increasing the step size leads to larger discrepancies

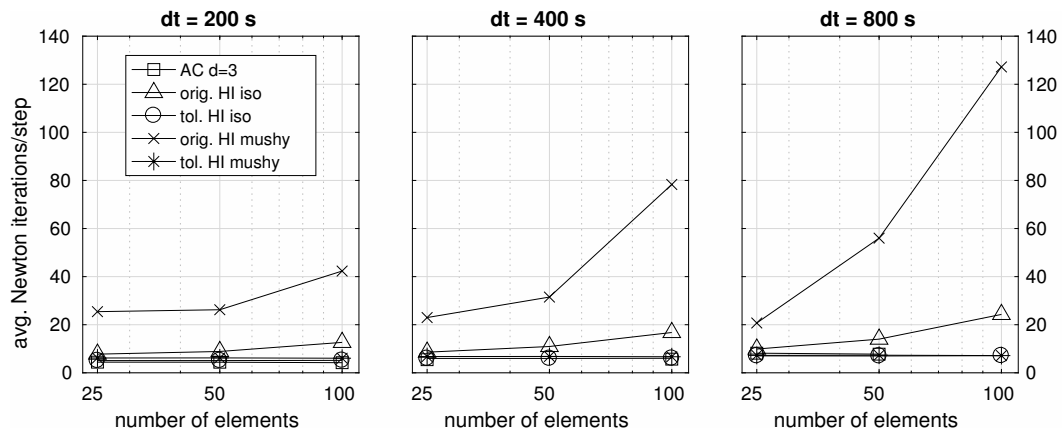


Fig. 12 Melting volume example: Average number of nonlinear iterations of all investigated methods for latent heat depending on spatial and temporal discretization.

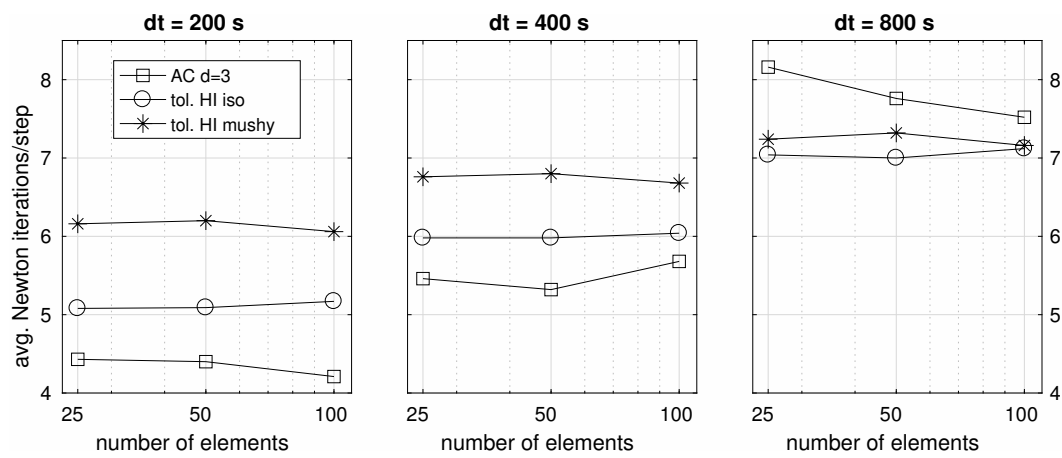


Fig. 13 Melting volume example: Average number of nonlinear iterations of best performing methods for latent heat depending on spatial and temporal discretization.

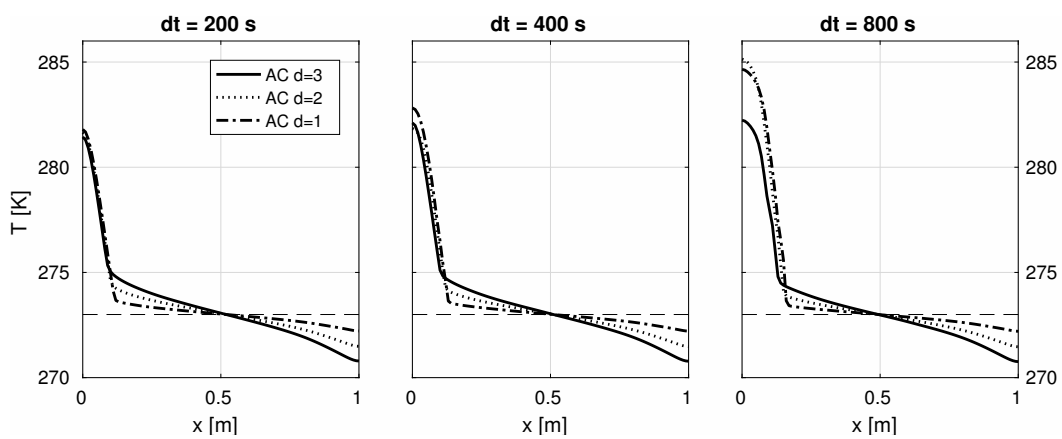


Fig. 14 Melting volume example: Temperature profiles at t_f obtained with AC methods for three time step sizes and with different phase change interval widths d . 100 elements.

in the maximum temperature. A smaller width d correlates with higher maximum temperatures which in turn implies that not all latent heat has been absorbed.

Summary of preliminary simulations: Taking into account all experience gathered from the two numerical examples, the authors recommend the use of the proposed tolerance-based HI method or an AC method. We found that the new criterion (22) to determine nodes that undergo phase change is superior to the one originally introduced by [36]. This is due to two reasons: first, the accuracy is user-controllable by setting a respective tolerance. Second, the new stopping criterion (22) typically leads to a significant reduction of nonlinear Newton iterations except for scenarios with very strict tolerances, which are, however, not expected to be necessary in the targeted application PBFAM.

Naturally, it is hard to predict a-priori which method will lead to less Newton iterations since this depends on the specific problem, tolerances and the (artificial) phase change interval width. Therefore, in the following, an actual example in the context of PBFAM will be investigated.

5.3 Single track scan

The following example simulates the scanning of a single track in a PBFAM process and was introduced in [13] and has also been simulated elsewhere, see [17]. A schematic sketch of the setup is shown in Fig. 15. A volumetric heat source described by Eq. (3) with effective power $W = 30$ W and size $R = 0.06$ mm is applied to the powder domain.

The geometry consists of a cuboid of $0.6 \times 0.2 \times 0.2$ mm³. The top layer of 0.05 mm in z -direction is in powder form and rests on top of a solid substrate domain. The material is a 316L type steel with parameters summarized in Tab. 2. The whole domain is initialized at a fixed temperature $T_0 = 303$ K. All surfaces are insulating, only $x = 0.6$ mm has an essential boundary condition $\hat{T} = T_0 = 303$ K.

The laser beam center moves from an initial position at $x = -0.06$ mm (one laser beam radius outside the domain) with a scanning speed of $v = 120$ mm/s in x -direction along the symmetry plane $y = 0$. The powder layer is discretized by a regular hexahedral mesh with element size $h_0 = 0.0025$ mm, i.e. $n_{\text{ele}}^z = 20$ elements across the powder layer height. In the substrate domain, a mesh with double element height in z -direction is applied. Moreover, an adaptive time stepping scheme is applied that halves the time step size if no convergence is achieved by the employed Newton-Raphson scheme (within a prescribed maximal number of iterations), and that doubles the step size again after four convergent time steps on the smaller step size level. As initial step size a value of $\Delta t^{(0)} = 1$ μ s has been chosen, which has been verified to yield a sufficiently small time discretization error.

Table 2 Material parameters for single track scan example [17].

Parameter	Description	Value	Unit
ρ_h	Hemispherical reflectivity	0.7	-
β_h	Extinction coefficient	60	mm ⁻¹
C_p	Heat capacity, powder	2.98	MJ/m ³ K
C_s	Heat capacity, solid	4.25	MJ/m ³ K
C_m	Heat capacity, melt	5.95	MJ/m ³ K
$k_p(T)$	Conductivity, powder	0.2@200, 0.3@1600	W/mK@K
k_c	Conductivity, solid/melt	20	W/mK
T_m	Melting temperature	1700	K
H_m	Latent heat of fusion	2.18	GJ/m ³

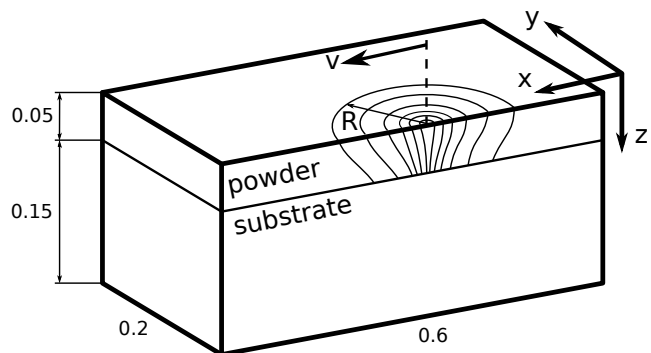


Fig. 15 Geometry and moving laser heat source for single track scan example [17]

Table 3 Comparison of maximum temperature and melt pool dimensions resulting from the different latent heat models.

Quantity	[13]	[17]	AC	HI
Max. temp. [K]	4900	5000	4990	4980
Length [mm]	0.30	0.27	0.28	0.29
Width [mm]	0.20	0.21	0.20	0.21
Depth [mm]	0.07	0.07	0.07	0.07

In prior simulations of this example, latent heat effects have been taken into account via an enthalpy method [13] and an isothermal HI method [17]. Here, we will use an AC method and subsequently the newly proposed tolerance-based isothermal HI scheme to simulate the process. An artificial melting interval is introduced for the AC method. As a baseline we chose $T_s = 1600$ K and $T_l = 1800$ K, i.e., $d = 100$ K. Isothermal HI is applied with a tolerance of $\epsilon_{\text{tol}} = 0.001$. The isothermal HI scheme is used in combination with enthalpy-based parameter interpolation, while the AC method is used with temperature-based interpolation. In a first step, qualitative characteristics of the solution shall be discussed. After a short period of time the melt pool shape reaches a steady-state. Its geometry can be visualized by the isotherm $T = T_m$. Fig. 16 compares the results obtained with the AC and tolerance-based HI method to the results reported in [13] and [17]. Both the AC and HI solution show good agreement with the reference. The melt pool dimensions

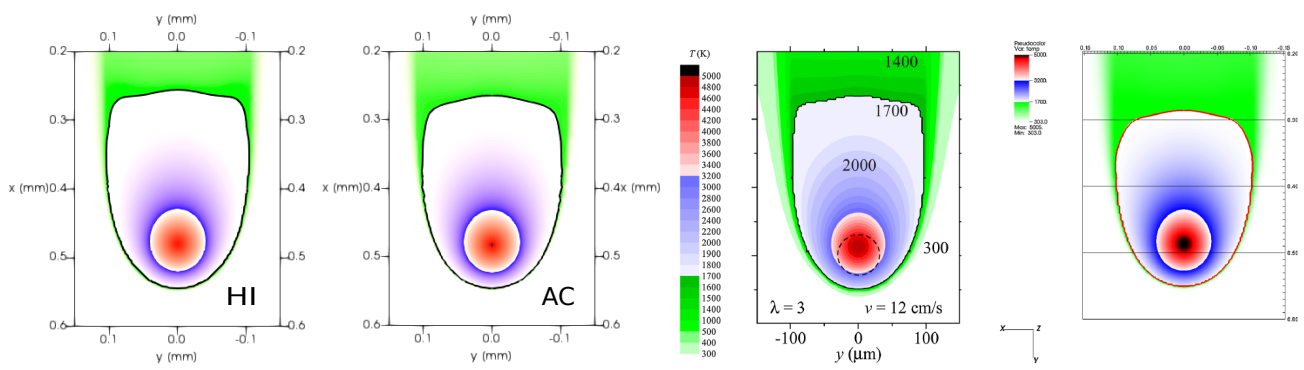


Fig. 16 Surface temperature profile and melt pool shape in steady-state. From left to right: current results from HI and AC scheme as well as reference results from Gusarov et al. [13] and Hodge et al. [17].

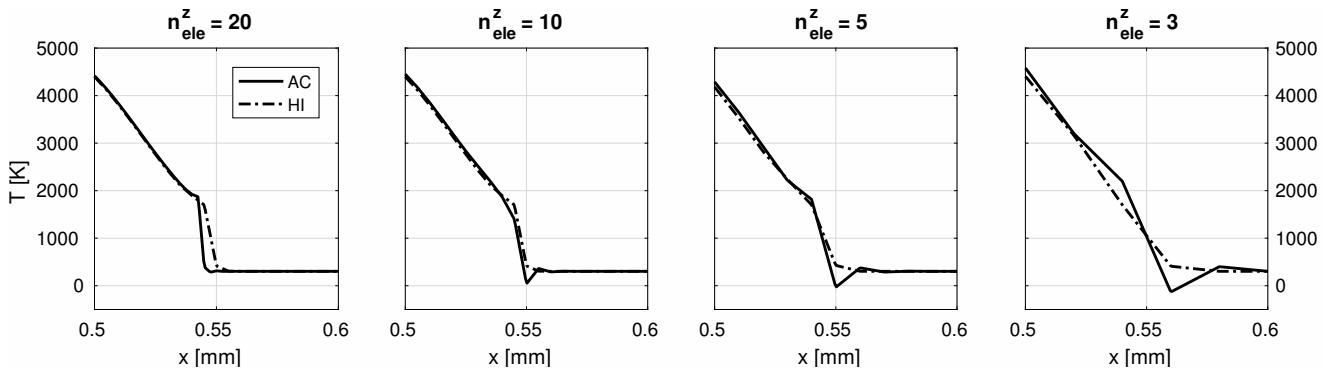


Fig. 17 Surface temperature profiles for AC and HI along laser path (i.e. $y = 0.0$ mm) for different spatial discretizations: Zoomed in to melting front of melt pool.

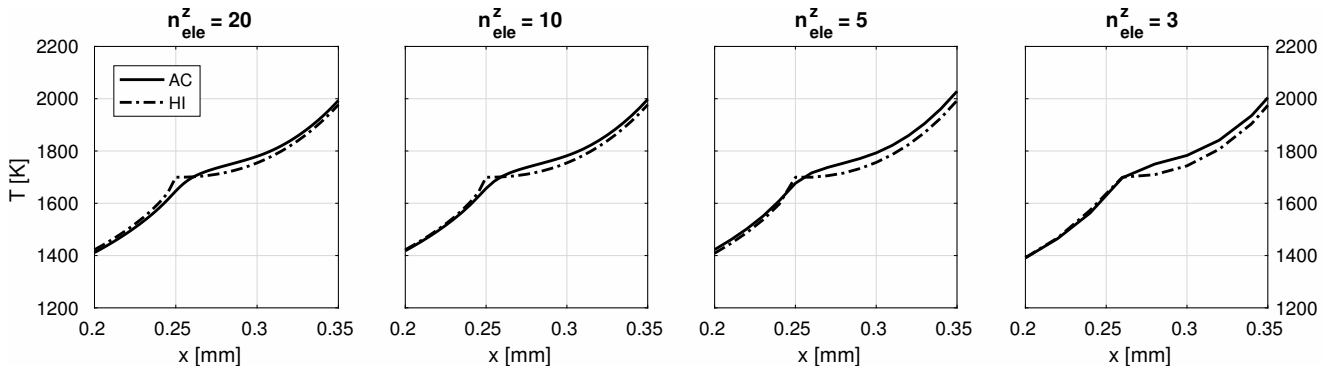


Fig. 18 Surface temperature profiles for AC and HI along laser path (i.e. $y = 0.0$ mm) for different spatial discretizations. Zoomed in to solidification region in melt pool tail.

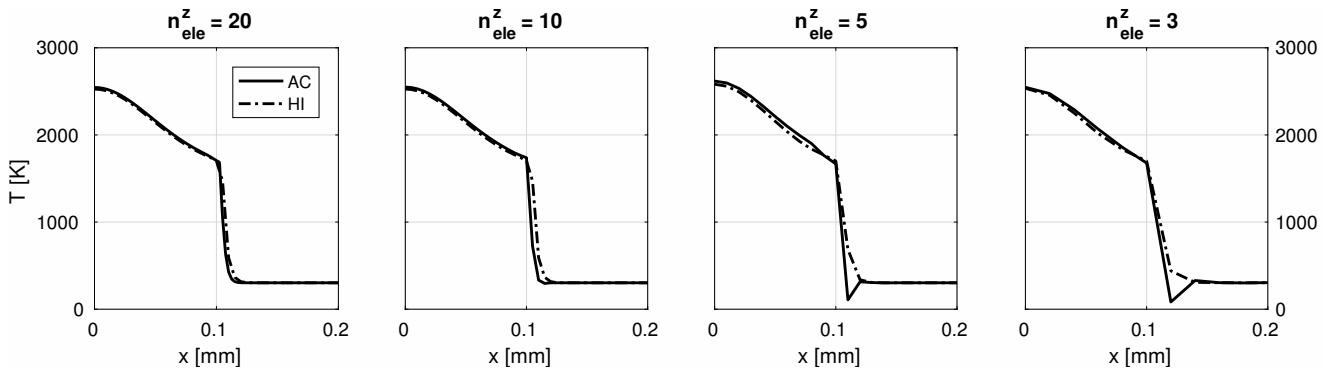


Fig. 19 Surface temperature profiles for AC and HI transverse to laser path at $x = 0.4$ mm showing transition from melt pool to powder.

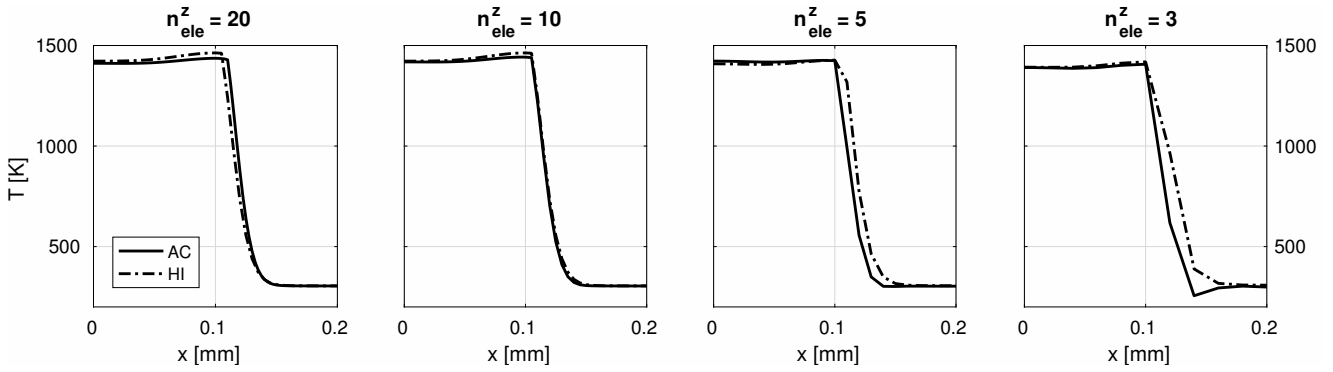


Fig. 20 Surface temperature profiles for AC and HI transverse to laser path at $x = 0.2$ mm showing transition from solid to powder.

and peak temperatures are compared quantitatively to the reference solutions in Tab. 3. All compared quantities show good agreement.

Since no more quantitative data is provided by the reference papers, we compare AC and HI method with each other. In the preliminary examples in Section 5.1 and 5.2 a strong dependency on spatial discretization was recognized. Three additional, coarser spatial discretizations with elements of size $2h_0$, $4h_0$ and $\frac{20}{3}h_0$ (which results in $n_{\text{ele}}^z \in \{10, 5, 3\}$ elements over the powder layer height) are introduced to investigate this phenomenon for the single track scan. The accuracy of both methods can be judged by looking at characteristic temperature profiles in the steady-state. All results presented in the following are shown for (approximately) $t = 4.6 \mu\text{s}$, which is the same point in time for which the melt pool shape has been illustrated in Fig. 16. First, Fig. 17 shows the surface temperature profiles for all discretizations plotted along the laser path (i.e. $y = 0$) in the vicinity of the melting front. This front is characterized by high temperature gradients and rates. With increasing element size, larger non-physical oscillations in the temperature profile are observed for the AC scheme. These oscillations can be traced back to the limitation of the employed first-order finite elements in representing strong gradients and material nonlinearities, here mainly caused by the extreme gradients of the thermal conductivity across the phase interface. No such oscillations occur with the HI scheme, which enforces the temperature in the phase transition region to lie within a temperature interval (implicitly) prescribed through the tolerance ϵ_{tol} . Although the shape functions used with the HI scheme are still first-order, the reset of temperature to a consistent melt temperature as described in (19) seems to prohibit temperature oscillations in the phase interface region as observed for AC, even though the HI scheme performs phase change and parameter interpolation within a considerably smaller temperature interval. It is important to note that so far the oscillations have not been observed to cause stability issues (e.g. a significant energy increase in the discrete system) and they remain small compared to the overall temperature range.

A second phase change happens along the laser path (i.e. $y = 0.0$ mm) when material cools down again at the tail of the melt pool. Fig. 18 gives a detailed view of the temperature profile in this region. The HI method produces a kink in the temperature profile at T_m , which is to be expected for a phase interface. The AC method produces a mushy phase change region and no kink is observed. However, further away both temperature profiles are in good agreement again.

Another aspect to investigate is the resulting temperature profile transverse to the laser scanning direction. Change from melt to powder can be investigated with a cut in y -direction at $x = 0.4$ mm as shown in Fig. 19. Again oscillations appear in the AC solution for coarser meshes but not in the HI solution. A similar picture emerges for a cut in y -direction through solid and powder, e.g. at $x = 0.2$ mm as illustrated in Fig. 20. In both transverse cuts temperature profiles differ for AC and HI method in proximity to T_m and agree well in some distance to the phase interface.

As suspected, in PBFAM applications the chosen method for latent heat only has a very local influence on the resulting temperature field, but does not significantly affect the global temperature characteristics from a rather macroscopic point of view. Another aspect of importance for PBFAM process simulations is numerical efficiency, here assessed in terms of nonlinear solver performance. Fig. 21 depicts the total number of Newton iterations accumulated over the whole simulation time for the different spatial discretizations. The results of the preliminary numerical examples in the previous sections seem to transfer to a larger example: the HI method shows a strong dependency on the spatial resolution, but in the practically relevant range of discretizations (e.g. 3 elements across the powder layer thickness), the difference becomes negligible.

In a next step, it shall be investigated how the accuracy and numerical efficiency of the two considered phase change schemes can be influenced by the respective numerical parameters d (phase change interval of the AC scheme) and ϵ (tolerance of the HI scheme). In a first step, the phase change interval for the AC method is varied for the two coarsest

spatial discretizations to see how it affects the temperature oscillation. It has to be noted that this also changes the temperature interval for temperature-based parameter interpolation. The intervals are given by $T_s = T_m - d$ and $T_l = T_m + d$, where $d \in \{100, 250, 500\}$ [K]. Moreover, two additional versions of HI with relaxed tolerances of $\epsilon_{\text{tol}} = 0.01$ and $\epsilon_{\text{tol}} = 0.1$ are simulated. The resulting surface temperatures are plotted in Fig. 22, 23 and 24 in the regions that showed oscillations in the previous plots. While the increased phase change interval for the AC decreases the amplitude of these oscillations by a certain amount, the overall accuracy of the temperature profiles decreases as well. Thus, it has to be concluded that for a given spatial discretization the width d of the phase change interval is not a suitable parameter to control the accuracy of AC schemes. The solutions obtained with different tolerances for the HI method show no oscillation. The solution from HI with tolerance $\epsilon_{\text{tol}} = 0.01$ is indistinguishable from the one with stricter tolerance $\epsilon_{\text{tol}} = 0.001$. The solution from HI with tolerance $\epsilon_{\text{tol}} = 0.1$ deviates slightly from the ones with stricter tolerances in the solid-powder transition region, see Fig. 24. However, it still seems to be considerably more accurate than the solution from AC with $d = 500$ K.

Finally, the initial time step size Δt^0 for the three considered HI and AC variants is increased up to 64 times of the original value. The total number of Newton iterations that is now required is depicted in Fig. 25. It is emphasized that the time step halving scheme is still employed. It was optimized individually for each method to yield low iteration counts. Moreover, it has been checked that the time discretization error is still sufficiently small, i.e. there is no visible difference in the results for base time step sizes up to 16 times Δt^0 for all variants. Higher step sizes lead to visible albeit small deviations in the temperature profiles, which are smaller, however, than the deviations resulting from the different HI and AC variants. According to Fig. 25, an increased phase change interval d in AC allows for larger step sizes and thus less iterations. Especially on the coarsest mesh, HI with a high tolerance ($\epsilon = 0.1$) yields a comparable number of accumulated Newton iterations, but at a considerably increased accuracy, as compared to the AC method with the (unphysically) large phase change interval $d = 500$ K. All in all, for a given spatial discretization, the proposed HI scheme allows to directly control numerical efficiency and accuracy by means of a user-defined tolerance. Within the considered scope of numerical examples and practically relevant spatial and temporal discretizations, this property made the novel tolerance-based HI scheme preferable as compared to the original HI scheme and the investigated AC method.

6 Conclusion

In this work, an extension of phase change and latent heat models for the simulation of metal powder bed fusion ad-

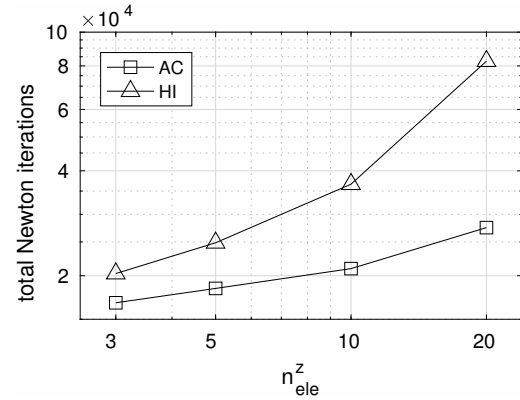


Fig. 21 Numerical efficiency of AC and HI in terms of total Newton iterations required.

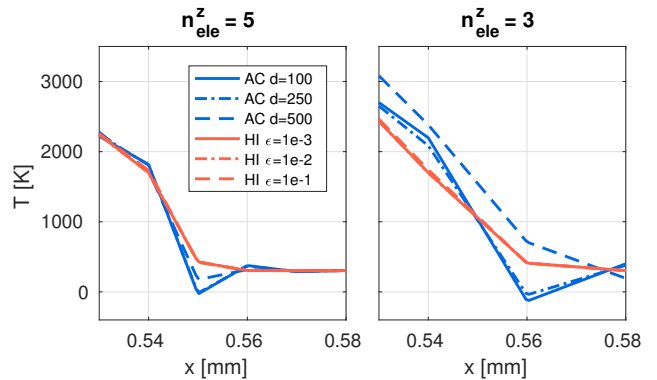


Fig. 22 Surface temperature profiles for AC with different phase change intervals along laser path (i.e. $y = 0.0$ mm): Zoomed in to melting front.

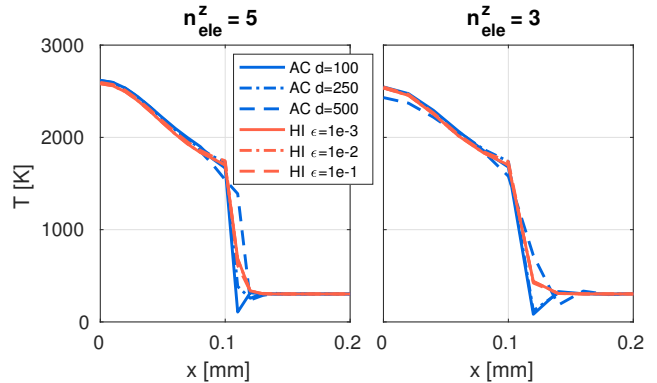


Fig. 23 Surface temperature profiles for AC with different phase change intervals transverse to laser path at $x = 0.4$ mm showing transition from melt pool to powder.

ditive manufacturing processes on the macroscale has been proposed and different models have been compared with respect to accuracy and numerical efficiency. In this context, a systematic formulation of phase fraction variables has been proposed relying either on temperature- or enthalpy-based interpolation schemes. Moreover, latent heat has been considered either by means of an apparent capacity (AC) or heat integration (HI) method. For the latter, a novel phase change

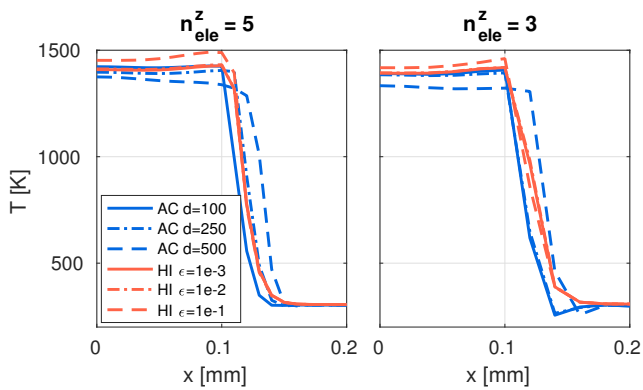


Fig. 24 Surface temperature profiles for AC with different phase change intervals transverse to laser path at $x = 0.2\text{mm}$ showing transition from solid to powder.

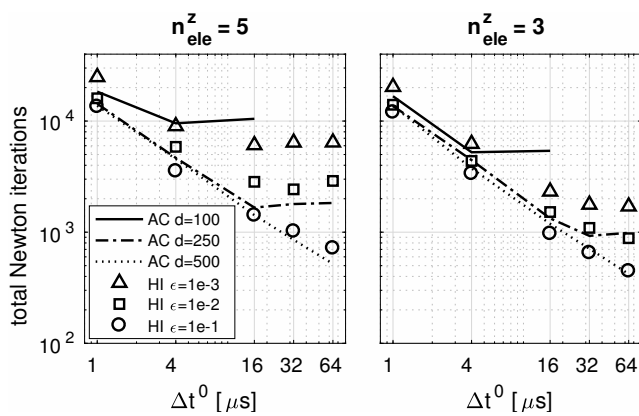


Fig. 25 Total number of Newton iterations required for different initial time step sizes Δt^0 in the time step halving scheme.

criterion has been proposed, which combines superior accuracy and numerical efficiency (in terms of an improved non-linear solver performance allowing for larger time step sizes and fewer iterations per time step) as compared to the original HI scheme. Compared to the AC approach, the numerical efficiency of the proposed tolerance-based HI scheme is comparable while offering an increased level of accuracy. Numerical results from the literature have been reproduced, which shows the validity of the proposed scheme. In summary, both the AC and the proposed tolerance-based HI scheme perform well when considering the accuracy requirements as well as practically relevant spatial and temporal discretization resolutions for PBFAM process simulation. Still, the authors believe that the new tolerance-based HI method is advantageous over AC schemes due to the user-controllable tolerance, which allows to directly control numerical efficiency and accuracy of the scheme, and which can directly be interpreted as the error in latent heat made during a phase change process.

For part-scale PBFAM models thermo-mechanical interaction is one of the primary interests. Structural parameters such as Young's modulus or the thermal expansion coefficient

may depend upon the temperature history in a similar fashion as proposed in the current work for the thermal parameters. Future research work will focus on the question of how the proposed methods for latent heat and parameter interpolation will behave in the thermo-mechanically coupled scenario.

References

- Bartel, T., Guschke, I., Menzel, A.: Towards the simulation of Selective Laser Melting processes via phase transformation models. *Computers & Mathematics with Applications* (2018). DOI 10.1016/j.camwa.2018.08.032
- Cervera, G.B.M., Lombra, G.: Numerical prediction of temperature and density distributions in selective laser sintering processes. *Rapid Prototyping Journal* **5**(1), 21–26 (1999)
- Chang, B., Allen, C., Blackburn, J., Hilton, P., Du, D.: Fluid Flow Characteristics and Porosity Behavior in Full Penetration Laser Welding of a Titanium Alloy. *Metallurgical and Materials Transactions B* **46**(2), 906–918 (2015)
- Childs, T.H., Hauser, G., Badrossamay, M.: Selective laser sintering (melting) of stainless and tool steel powders: Experiments and modelling. *Proceedings of the Institution of Mechanical Engineers, Part B: Journal of Engineering Manufacture* **219**(4), 339–357 (2005)
- Comini, G., Del Giudice, S., Lewis, R.W., Zienkiewicz, O.C.: Finite element solution of non-linear heat conduction problems with special reference to phase change. *International Journal for Numerical Methods in Engineering* **8**(3), 613–624 (1974)
- Denlinger, E.R., Heigel, J.C., Michaleris, P.: Residual stress and distortion modeling of electron beam direct manufacturing Ti-6Al-4V. *Proceedings of the Institution of Mechanical Engineers, Part B: Journal of Engineering Manufacture* **229**(10), 1803–1813 (2015)
- Denlinger, E.R., Irwin, J., Michaleris, P.: Thermomechanical Modeling of Additive Manufacturing Large Parts. *Journal of Manufacturing Science and Engineering* **136**(6), 61007 (2014)
- Geiger, M., Leitz, K.H., Koch, H., Otto, A.: A 3D transient model of keyhole and melt pool dynamics in laser beam welding applied to the joining of zinc coated sheets. *Production Engineering* **3**(2), 127–136 (2009)
- Gibson, I., Rosen, D., Stucker, B.: *Additive Manufacturing Technologies*. Springer New York, New York, NY (2015)
- Gong, X., Chou, K.: Phase-Field Modeling of Microstructure Evolution in Electron Beam Additive Manufacturing. *JOM* **67**(5), 1176–1182 (2015)
- Gusarov, A., Kruth, J.P.: Modelling of radiation transfer in metallic powders at laser treatment. *International Journal of Heat and Mass Transfer* **48**(16), 3423–3434 (2005)
- Gusarov, A.V.: Homogenization of radiation transfer in two-phase media with irregular phase boundaries. *Physical Review B - Condensed Matter and Materials Physics* **77**(14), 1–14 (2008)
- Gusarov, A.V., Yadroitsev, I., Bertrand, P., Smurov, I.: Model of Radiation and Heat Transfer in Laser-Powder Interaction Zone at Selective Laser Melting. *Journal of Heat Transfer* **131**(7), 72101 (2009)
- Herbold, E.B., Walton, O., Homel, M.A.: Simulation of Powder Layer Deposition in Additive Manufacturing Processes Using the Discrete Element Method. Tech. rep., Lawrence Livermore National Laboratory (LLNL), Livermore, CA (United States) (2015)
- Herzog, D., Seyda, V., Wycisk, E., Emmelmann, C.: Additive manufacturing of metals. *Acta Materialia* **117**, 371–392 (2016)
- Hodge, N., Ferencz, R., Vignes, R.: Experimental comparison of residual stresses for a thermomechanical model for the simulation of selective laser melting. *Additive Manufacturing* **12**, 159–168 (2016)

17. Hodge, N.E., Ferencz, R.M., Solberg, J.M.: Implementation of a thermomechanical model for the simulation of selective laser melting. *Computational Mechanics* **54**(1), 33–51 (2014)
18. Hu, H., Argyropoulos, S.A.: Mathematical modelling of solidification and melting: A review. *Modelling and Simulation in Materials Science and Engineering* **4**(4), 371–396 (1996)
19. Jamshidinia, M., Kong, F., Kovacevic, R.: Temperature Distribution and Fluid Flow Modeling of Electron Beam Melting® (EBM). In: Volume 7: Fluids and Heat Transfer, Parts A, B, C, and D, p. 3089. ASME (2013)
20. Khairallah, S.A., Anderson, A.: Mesoscopic simulation model of selective laser melting of stainless steel powder. *Journal of Materials Processing Technology* **214**(11), 2627–2636 (2014)
21. Kollmannsberger, S., Carraturo, M., Reali, A., Auricchio, F.: Accurate Prediction of Melt Pool Shapes in Laser Powder Bed Fusion by the Non-Linear Temperature Equation Including Phase Changes. *Integrating Materials and Manufacturing Innovation* **8**(2), 167–177 (2019)
22. Kollmannsberger, S., Özcan, A., Carraturo, M., Egger, J., Schröder, A., Rank, E.: A multi-level model for the simulation of AM processes. In: *Simulation for Additive Manufacturing* (2017)
23. Körner, C., Attar, E., Heinel, P.: Mesoscopic simulation of selective beam melting processes. *Journal of Materials Processing Technology* **211**(6), 978–987 (2011)
24. Lindgren, L.E., Lundbäck, A., Fisk, M., Pederson, R., Andersson, J.: Simulation of additive manufacturing using coupled constitutive and microstructure models. *Additive Manufacturing* **12**, 144–158 (2016)
25. Markl, M., Ammer, R., Rude, U., Körner, C.: Numerical investigations on hatching process strategies for powder-bed-based additive manufacturing using an electron beam. *International Journal of Advanced Manufacturing Technology* **78**(1-4), 239–247 (2015)
26. Meier, C., Penny, R.W., Zou, Y., Gibbs, J.S., Hart, A.J.: Thermo-physical Phenomena In Metal Additive Manufacturing By Selective Laser Melting: Fundamentals, Modeling, Simulation, And Experimentation. *Annual Review of Heat Transfer* **20**(1), 241–316 (2017)
27. Meier, C., Weissbach, R., Weinberg, J., Wall, W.A., Hart, A.J.: Critical influences of particle size and adhesion on the powder layer uniformity in metal additive manufacturing. *Journal of Materials Processing Technology* **266**, 484–501 (2019)
28. Meier, C., Weissbach, R., Weinberg, J., Wall, W.A., John Hart, A.: Modeling and characterization of cohesion in fine metal powders with a focus on additive manufacturing process simulations. *Powder Technology* **343**, 855–866 (2019)
29. de Moraes, D., Czekanski, A.: Parametric Thermal FE Analysis on the Laser Power Input and Powder Effective Thermal Conductivity during Selective Laser Melting of SS304L. *Journal of Manufacturing and Materials Processing* **2**(3), 47 (2018)
30. Morgan, K., Lewis, R.W., Zienkiewicz, O.C.: An improved algorithm for heat conduction problems with phase change. *International Journal for Numerical Methods in Engineering* **12**(7), 1191–1195 (1978)
31. Neiva, E., Badia, S., Martín, A.F., Chiumenti, M.: A scalable parallel finite element framework for growing geometries. Application to metal additive manufacturing. *International Journal for Numerical Methods in Engineering* (2019). DOI 10.1002/nme.6085
32. Oliveira, B., Afonso, J.C., Zlotnik, S.: A Lagrangian-Eulerian finite element algorithm for advection-diffusion-reaction problems with phase change. *Computer Methods in Applied Mechanics and Engineering* **300**, 375–401 (2016)
33. Rai, A., Markl, M., Körner, C.: A coupled Cellular Automaton-Lattice Boltzmann model for grain structure simulation during additive manufacturing. *Computational Materials Science* **124**, 37–48 (2016)
34. Rai, R., Burgardt, P., Milewski, J.O., Lienert, T.J., Debroy, T.: Heat transfer and fluid flow during electron beam welding of 21Cr-6Ni-9Mn steel and Ti-6Al-4V alloy. *Journal of Physics D: Applied Physics* **42**(2) (2009)
35. Riedlbauer, D., Scharowsky, T., Singer, R.F., Steinmann, P., Körner, C., Mergheim, J.: Macroscopic simulation and experimental measurement of melt pool characteristics in selective electron beam melting of Ti-6Al-4V. *International Journal of Advanced Manufacturing Technology* **88**(5-8), 1309–1317 (2017)
36. Rolph, W.D., Bathe, K.J.: An efficient algorithm for analysis of nonlinear heat transfer with phase changes. *International Journal for Numerical Methods in Engineering* **18**(1), 119–134 (1982)
37. Roy, S., Juha, M., Shephard, M.S., Maniatty, A.M.: Heat transfer model and finite element formulation for simulation of selective laser melting. *Computational Mechanics* **62**(3), 273–284 (2018)
38. Russell, M.A., Souto-Iglesias, A., Zohdi, T.I.: Numerical simulation of Laser Fusion Additive Manufacturing processes using the SPH method. *Computer Methods in Applied Mechanics and Engineering* **341**, 163–187 (2018)
39. Salsi, E., Chiumenti, M., Cervera, M.: Modeling of Microstructure Evolution of Ti6Al4V for Additive Manufacturing. *Metals* **8**(8), 633 (2018)
40. Shen, N., Chou, K.: Numerical Thermal Analysis in Electron Beam Additive Manufacturing With Preheating Effects. *Proceedings of the 23rd Solid Freeform Fabrication Symposium* pp. 774–784 (2012)
41. Wall, W., Popp, A., Kronbichler, M., Mayr, M., Meier, C., Vuong, A.T., Ager, C., Bräu, F., Grill, M.: BACI: A multiphysics simulation environment. Tech. rep., Institute for Computational Mechanics, Technische Universität München (2019)
42. Wessels, H., Weißenfels, C., Wriggers, P.: Metal particle fusion analysis for additive manufacturing using the stabilized optimal transportation meshfree method. *Computer Methods in Applied Mechanics and Engineering* **339**, 91–114 (2018)
43. Yan, W., Qian, Y., Ge, W., Lin, S., Liu, W.K., Lin, F., Wagner, G.J.: Meso-scale modeling of multiple-layer fabrication process in Selective Electron Beam Melting: Inter-layer/track voids formation. *Materials and Design* **141**, 210–219 (2018)
44. Zaeh, M.F., Branner, G.: Investigations on residual stresses and deformations in selective laser melting. *Production Engineering* **4**(1), 35–45 (2010)
45. Zhang, J., Liou, F., Seufzer, W., Newkirk, J., Fan, Z., Liu, H., Sparks, T.E.: Probabilistic Simulation of Solidification Microstructure Evolution During Laser-Based Metal Deposition. *Proceedings of the Solid Freeform Fabrication Symposium* pp. 739–748 (2013)
46. Zhang, Y., Guillemot, G., Bernacki, M., Bellet, M.: Macroscopic thermal finite element modeling of additive metal manufacturing by selective laser melting process. *Computer Methods in Applied Mechanics and Engineering* **331**, 514–535 (2018)